International Journal of Engineering and Technology Innovation, vol. 14, no. 4, 2024, pp. 389-406

Proactive Prevention Strategies for Grid Risk Scenarios Based on Pumped Storage Participation

Hui-Qing Deng[1,2,*], Hui Wu[1], Zhi-Wei Liang[1], Pang-Rong Zheng[1], Jun-Fu Shen[1]

[1]School of Electronic, Electrical Engineering and Physics, Fujian University of Technology, Fuzhou, Fujian Province, China

[2]Fujian University Engineering Research Center for Simulation Analysis and Integrated Control of Smart Grid, Fuzhou, Fujian Province, China

Received 25 April 2024; received in revised form 30 May 2024; accepted 31 May 2024

DOI: https://doi.org/10.46604/ijeti.2024.13635

Abstract

Given the increasing importance of cascading trip prevention, this study presents the pumped storage characteristics to cooperate with thermal units and further ensure the safety of grid operation. The proposed model comprises two phases: the first phase is the day-ahead decision-making phase, which synergistically optimizes thermal units and pumped storage to improve the flexibility of grid operation; the second phase is the intra-day adjustment phase considering the uncertainty of the wind-photovoltaic and transmission line failure outage to enhance the robustness. Furthermore, this model employs a column and constraint generation algorithm to solve the two-phase, three-layer optimization problem, thereby minimizing the adjustment cost under the riskiest scenarios. The experimental results show that adding pumped storage reduces the total system operating cost by 3.99%, the renewable energy abandonment rate to 0.65%, and the thermal power unit output standard deviation to 74.13 MW.

Keywords: transmission line, electric betweenness, pumped storage, cascading tripping, uncertainty

1. Introduction

With the proposal of the "double carbon" goal, the rapid expansion of clean energy sources such as wind power and photovoltaic power is evident [1-2]. Relevant projections suggest that by 2030, the cumulative installed capacity of wind-photovoltaic power in China will surpass 1.2 billion kilowatts, constituting over 50% of the total installed power capacity [3]. However, the growing integration of wind-photovoltaic power into the grid poses challenges due to its inherent volatility and intermittency, thereby augmenting the complexity and uncertainty within the power system. As a result, ensuing susceptibility to cascading failures is heightened. Multi-energy complementarity strategies are predominantly utilized to mitigate the variability and instantaneous fluctuations, which are associated with wind-photovoltaic power. Moreover, pumped storage renders itself notable as a premier regulation and energy storage method, crucial for supporting the evolving power grid [4-5]. Nonetheless, optimizing the integration of pumped storage within the multi-source energy system is hindered concerning the risk mitigation of cascading failures while maximizing system benefits.

Reserve operation of thermal power units and demand-side response mechanisms represent effective strategies for ensuring the stability of power system operations. However, the escalating integration of renewable energy sources into the grid, such as wind-photovoltaic power, introduces high uncertainty, potentially compromising the efficacy of conventional reserve approaches. Consequently, extensive research endeavors have been undertaken to optimize unit reserve strategies. A

* Corresponding author. E-mail address: 2221905075@smail.fjut.edu.cn

English language proofreader: Chih-Wei Chang

two-stage optimal scheduling framework, as mentioned in Cao et al. [6], is introduced for thermal power plants spanning the day-ahead and intraday horizons, incorporating considerations of both electrical energy efficiency and reserve benefits. Meanwhile, a novel reserve method, as shown in Zhang et al. [7], is proposed for integrating renewable energy sources into the grid, assessing its impact on grid scheduling operations regarding grid security and renewable energy utilization.

To discuss further, a flexible reserve optimization model is formulated by Li et al. [8], and this model is grounded in conditional value-at-risk principles while accounting for worst-case operational scenarios. Finally, a wind-thermal coordinated reserve strategy, as indicated by Lin et al. [9], is developed to evaluate its performance across panoply operational states within wind farms. Pumped storage systems are instrumental in enhancing the utilization of renewable energy resources, facilitating consistent power output, and enhancing frequency and voltage regulation [10-12]. In addition to positive effects, pumped storage systems are capable of addressing various grid challenges, including emergency power provision, peak load management, frequency regulation, and optimization of tidal currents, thereby bolstering grid safety and stability [13]. On the demand side, pumped storage is a reliable backup power source during system disturbances, ensuring the continuity and reliability of the power supply [14]. However, more research has yet to be conducted thus far on harnessing the potential of pumped storage systems to mitigate power grid chain failures.

Modeling approaches for scenarios, that involve uncertainties in scenery and transmission line failures, primarily encompass scenario-based stochastic optimization and robust optimization techniques. Robust optimization, in particular, has garnered significant attention and pervasively investigated due to its inherent advantages. Unlike scenario-based approaches, robust optimization does not necessitate explicit scenario acquisition, circumventing extensive data processing requirements. Moreover, such an optimization effectively accommodates operational constraints imposed by stochastic scenarios, thereby bolstering the stability of power systems. A resilient response framework integrated within a smart grid is presented, which is formulated using a two-stage robust mixed integer optimization model [15]. This framework enhances the resilience of the system against transmission line outages during disaster scenarios.

Similarly, a robust optimization model is proposed for Security-Constrained Unit Commitment (SCUC), which aims to enhance the operational reliability of Integrated Energy Grid Systems (IEGS) in the event of transmission line failures [16]. Additionally, a robust scheduling model is introduced for wind power load shedding and reserve operations, effectively mitigating the volatility of wind power output and alleviating system reserve pressures [17]. A two-stage robust optimization considering demand response and safety performance has been proposed [18-20]. However, it is noteworthy that most existing studies primarily focus on modeling either the uncertainty associated with renewable energy output or the risk of transmission line failures individually, without concurrently considering the combined impact of these two critical risk factors on the secure dispatch operation of the grid.

By addressing current shortcomings, this paper introduces a novel approach to mitigate chain failures by integrating pumped storage and conventional unit reserve while accounting for uncertainties in wind-photovoltaic power output and the repercussions of transmission line failures on grid safety.

2. Establishment of Risk-Prone Operational Scenarios

In this study, the risk operation scenario model incorporates the potential occurrence of transmission line faults, inherent randomness, and variability in the output of wind and photovoltaic renewable energy sources. The deterministic and uncertain set U can be mathematically expressed, as depicted in the formula. The complexity of the modeled operational scenarios increases with the size of this uncertainty set, necessitating diverse scheduling strategies for pumped storage to balance economic considerations with reliability concerns effectively.

2.1. Transmission line failure outage

This paper employs the electric betweenness method to identify critical branches within the network for potential outages, as these branches serve as out-of-service lines. The electric betweenness is a robust metric for assessing the structural integrity of the network. However, given that the primary function of the grid is to facilitate the transmission of tidal currents, a comprehensive evaluation of its performance requires both its internal structural characteristics and the dynamics of tidal currents. Electric betweenness properties emerge as pivotal factors in assessing risky operational scenarios, as they equalize the interplay between current magnitude and grid structure, thereby contributing to a profound insight into grid performance.

Apropos a network comprising M branches and N nodes, with a designated set of load nodes L and generator nodes G, the electric betweenness $B_e(m,n)$ for line (m,n) delineates the current contribution between load-generator node pairs and characterizes the capacity of the branch for current propagation throughout the network. Such a process is mathematically defined as:

$$B_e(m,n) = \sum_{i\in G,\, j\in L} \sqrt{W_i W_j}\left|I_{ij}(m,n)\right| \tag{1}$$

where $I_{ij}(m,n)$ is the current generated on line (m,n) after injecting a unit current between the generator-load node pair (i,j); W_i is the weight of generator node i, which is adopted as the rated capacity of the generator or the actual output; W_j is the weight of the load node j, which represents the actual or the peak load value; L and G are the set of load nodes and generator nodes, respectively.

2.2. Renewable energy output stochasticity

Given the relatively lower accuracy of wind and photovoltaic power predictions, compared to traditional load forecasts, this study examines spatiotemporal uncertainties and their implications for grid operation. Specifically, temporal uncertainty (denoted by Π_t) refers to the frequency of power fluctuations in wind and photovoltaic sources, while spatial uncertainty (represented by Π_ω and Π_v) refers to the number of simultaneous power fluctuations across wind farms and photovoltaic stations within the grid.

$$A_{\omega,t}^{s} = A_{\omega,t}^{0} + Z_{\omega,t}^{+}\left(A_{\omega,t}^{\max} - A_{\omega,t}^{0}\right) - Z_{\omega,t}^{-}\left(A_{\omega,t}^{0} - A_{\omega,t}^{\min}\right) \tag{2}$$

$$A_{v,t}^{s} = A_{v,t}^{0} + Z_{v,t}^{+}\left(A_{v,t}^{\max} - A_{v,t}^{0}\right) - Z_{v,t}^{-}\left(A_{v,t}^{0} - A_{v,t}^{\min}\right) \tag{3}$$

$$Z_{\omega,t}^{+} + Z_{\omega,t}^{-} \le 1;\ Z_{v,t}^{+} + Z_{v,t}^{-} \le 1 \tag{4}$$

$$\sum_{t=1}^{N_t}\left(Z_{\omega,t}^{+} + Z_{\omega,t}^{-}\right) \le \Pi_t;\ \sum_{t=1}^{N_t}\left(Z_{v,t}^{+} + Z_{v,t}^{-}\right) \le \Pi_t \tag{5}$$

$$\sum_{\omega=1}^{N_\omega}\left(Z_{\omega,t}^{+} + Z_{\omega,t}^{-}\right) \le \Pi_\omega;\ \sum_{v=1}^{N_v}\left(Z_{v,t}^{+} + Z_{v,t}^{-}\right) \le \Pi_v \tag{6}$$

where N_ω and N_v are the number of wind farms and photovoltaic stations, respectively; the superscript "s" is defined as the physical quantity of the intraday phase; $A_{\omega,t}^{max}$ and $A_{\omega,t}^{min}$ are the maximum and minimum values of wind power available at wind farms ω at time t, respectively; $A_{v,t}^{max}$ and $A_{v,t}^{min}$ are the maximum and minimum values of photovoltaic stations v at time t, respectively; $Z_{\omega,t}^{+}$ and $Z_{\omega,t}^{-}$ are state variables, with 0-1 integers to characterize whether the wind farm fluctuates; $Z_{v,t}^{+}$ and $Z_{v,t}^{-}$ are state variables with 0-1 integers to characterize whether the photovoltaic stations fluctuate; Π_t, Π_ω, and Π_v are denoted as uncertainty sets; Eqs. (2)-(4) indicate that the intraday phase wind $A_{\omega,t}^{s}$, photovoltaic $A_{v,t}^{s}$ consist of upward/downward fluctuations of wind and photovoltaic superimposed on their forecasts $A_{\omega,t}^{0}$ and $A_{v,t}^{0}$. Eqs. (5)-(6) are expressed as the temporal and spatial uncertainties of wind and photovoltaic, respectively.

3. Active Prevention and Control Against Power Grid Cascading Tripping

The active prevention and control model for the involvement of pumped storage is structured as a two-stage, three-layer optimization framework spanning the day-ahead and intraday periods. Specifically, this comprehensive model integrates wind power, photovoltaic, thermal power, and pumped storage units, as illustrated in Fig. 1.

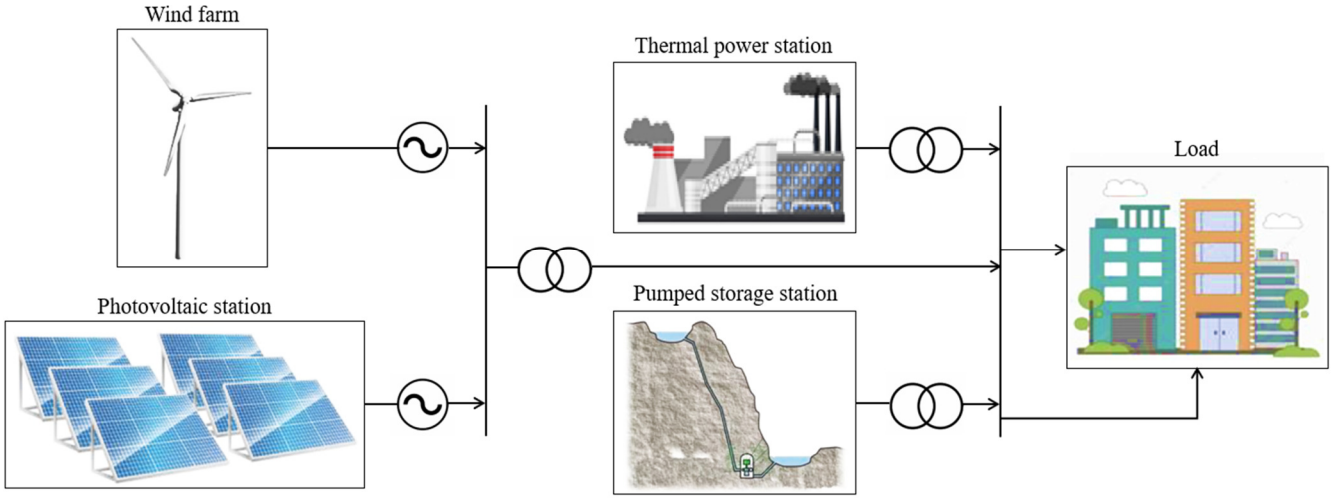

Fig. 1 Wind-photovoltaic-thermal-pumping storage combined system

During the day-ahead stage, conventional scheduling techniques are employed to minimize unit operation costs and reserve expenditures, considering the predicted output of wind power and photovoltaic sources. This stage entails determining the operational mode of thermal power units and allocating reserves to mitigate potential risk scenarios in the subsequent intraday phase. The reserve capacity encompasses thermal power unit reserves and pumps the peak shaving of storage and valley filling capabilities. In the intraday phase, backup resources are activated to ensure system safety amid deterministic and uncertain scenarios, which can be identified during risk assessment. The optimization process minimizes the overall system cost by identifying and addressing the most severe risk scenarios while averting cascading failures. The collaborative resolution of the two-stage optimization problem guarantees operational economic efficiency and reliability. The objective function of the model is represented by:

$$\min C_{main} + \max_{U} \min C_{sub} \tag{7}$$

where C_{main} signifies the optimization objective for the day-ahead phase; C_{sub} represents the optimization objective for the intraday phase; and U symbolizes the set of both certainty and uncertainty in the risky operating scenario, including wind and photovoltaic uncertainty and transmission line fault outages.

3.1. Day-ahead stage optimization

(1) Objective function

$$\begin{aligned}\min C_{main} = &\sum_{t=1}^{N_T}\sum_{g=1}^{N_G}\left(F_g(P_{g,t}^0) + C_g^{R+}R_{g,t}^{+} + C_g^{R-}R_{g,t}^{-} + C_g^{U} + C_g^{D}\right) \\ &+\sum_{t=1}^{T_{e,t}}\sum_{i=1}^{N_H} F_{e,t}(e_{i,t}^0)y_{e,i,t} - \sum_{t=1}^{T_{p,t}}\sum_{i=1}^{N_H} F_{p,t}(p_{i,t}^0)y_{p,i,t}\end{aligned} \tag{8}$$

where N_G and N_H stand for the number of thermal power units and pumped storage units, respectively; $P_{g,t}^0$ signifies the g output of thermal power units at the moment of t, $e_{i,t}^0$ and $p_{i,t}^0$ denote the generation power and pumping power of pumped storage units at the moment of t, respectively, and "0" means the physical quantity of the day-ahead stage; $F_g(\cdot)$ stands for the

cost of coal consumption of thermal power units; C_g^U and C_g^D symbolize the startup/shutdown cost of thermal power units g, respectively; $R_{g,t}^+$ and $R_{g,t}^-$ are specified to be the up/down reserve capacity provided by thermal power unit g, respectively; C_g^{R+} and C_g^{R-} are designated as the up/down costs of thermal power unit g, respectively; $T_{e,t}$ and $T_{p,t}$ are defined as the generation and pumping time sets of pumped storage unit i, respectively; $y_{e,i,t}$ and $y_{p,i,t}$ are expressed as the state variables of generation and pumping conditions of pumped storage unit i at time t, respectively; $F_{e,t}(\cdot)$ and $F_{p,t}(\cdot)$ indicates the generation and pumping cost functions of pumped storage unit i, respectively.

(2) Coal consumption cost

$$F_g(P_{g,t}^0) = a_g(P_{g,t}^0)^2 + b_g P_{g,t}^0 + c_g \tag{9}$$

where a_g, b_g, and c_g are delineated as coal consumption factors.

In the optimization model devised for a small-scale node system, the coal consumption cost is represented as a quadratic function, as depicted in Eq. (9). However, as the system scale expands, particularly when the number of nodes exceeds 1000, the computational time required for the solution significantly escalates, leading to attenuated efficiency. To address this challenge, this study linearizes the original model by segmenting the nonlinear coal consumption cost function of thermal power units into m_0 segments. The original model specified in Eq. (9) is replaced with the formula below, as illustrated in Fig. 2.

$$F_g(P_{g,t,n}^0, u_{g,t}) = \sum_{n=1}^{m_0} K_{g,n} P_{g,t,n}^0 + u_{g,t} F_{g,0} \tag{10}$$

$$\begin{cases} F_{g,0} = a_g P_{g,\min}^2 + b_g P_{g,\min} + c_g \\ 0 \le P_{g,t,n}^0 \le \dfrac{P_{g,\max} - P_{g,\min}}{m_0} \\ P_{g,t}^0 = \sum_{n=1}^{m_0} P_{g,t,n}^0 + P_{g,\min} \end{cases} \tag{11}$$

where $K_{g,n}$ denotes the slope of each segment of the coal consumption function after linearization of the thermal unit; $P_{g,\max}$ and $P_{g,\min}$ are defined as the maximum and minimum output of the thermal unit, respectively; $F_{g,0}$ signifies the coal consumption generated by the thermal unit g turned on and operated at the minimum output; $P_{g,t,n}^0$ stands for the segmented output of the unit g at the moment of t; $u_{g,t}$ is rendered as the state of startup and shutdown of the thermal unit g, which is denoted by the 0-1 variable.

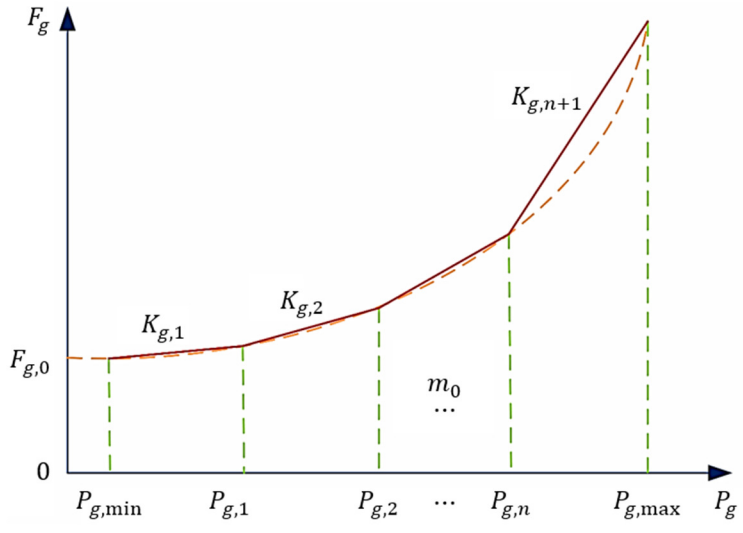

Fig. 2 Segmental linearization of fuel cost curves for thermal power units

(3) Thermal unit startup and shutdown cost constraints

$$\begin{cases} C_{g,t}^{U} \geq H_g (u_{g,t} - u_{g,t-1}) \\ C_{g,t}^{U} \geq 0 \end{cases} \tag{12}$$

$$\begin{cases} C_{g,t}^{D} \geq J_g (u_{g,t-1} - u_{g,t}) \\ C_{g,t}^{D} \geq 0 \end{cases} \tag{13}$$

where H_g and J_g are depicted as startup/shutdown costs of thermal power unit g.

(4) Thermal unit minimum startup/shutdown time constraints

$$\left(u_{g,t-1} - u_{g,t}\right)\left(T_{g,t-1} - T_{g,on}\right) \geq 0 \tag{14}$$

$$\left(u_{g,t} - u_{g,t-1}\right)\left(-T_{g,t-1} - T_{g,off}\right) \geq 0 \tag{15}$$

where $T_{g,on}$ and $T_{g,off}$ are designated as the startup/shutdown times of thermal power unit g.

(5) Power balance constraints

$$\sum_{g \in G_b} P_{g,t}^{0} + \sum_{\omega \in W_b} P_{\omega,t}^{0} + \sum_{v \in V_b} P_{v,t}^{0} + \sum_{i \in I_b} e_{i,t}^{0} - \sum_{i \in I_b} p_{i,t}^{0} = \sum_{l:o_2(l)=b} P_{l,t}^{0} - \sum_{l:o_1(l)=b} P_{l,t}^{0} \tag{16}$$

where G_b, W_b, V_b, and I_b symbolize the aggregation of thermal power units, wind farms, photovoltaic stations, and pumped storage connected to bus b, respectively; $l: o_1(l) = b$ and $l: o_2(l) = b$ signify the transmission lines injecting and discharging power from bus b, respectively; $P_{\omega,t}^{0}$ and $P_{v,t}^{0}$ indicate the dissipation of wind farm ω and photovoltaic stations v at the moment of t, respectively; $P_{l,t}^{0}$ is defined as the transmission power of line l at the moment of t, with the plus or minus representing the direction; $L_{b,t}$ is the load at node b at the moment of t.

(6) Line phase angle, power flow security constraints

$$P_{l,t}^{0} = \frac{\theta_{o_1(l),t}^{0} - \theta_{o_2(l),t}^{0}}{x_l} \tag{17}$$

$$-P_{l}^{\max} \leq P_{l,t}^{0} \leq P_{l}^{\max} \tag{18}$$

$$\underline{\theta} \leq \theta_{b,t}^{0} \leq \overline{\theta} \tag{19}$$

$$\theta_{\text{ref},t}^{0} = 0 \tag{20}$$

where $\theta_{o_1(l),t}^{0}$ and $\theta_{o_2(l),t}^{0}$ are expressed to be the voltage phase angles of the transmission line l injection and outflow buses at the moment t, respectively; x_l acts as the reactance value of line l; $P_l^{\max}$ represents the upper limit of the transmitted power of the transmission line l; $\overline{\theta}$ and $\underline{\theta}$ are specified as the upper and lower values of the voltage phase angle $\theta_{b,t}^{0}$ at the node b at the moment t, respectively; and $\theta_{\text{ref},t}^{0}$ means the voltage phase angle of the balancing node. Eqs. (17)-(18) delineate the power flow security constraints, and Eqs. (19)-(20) expound the phase angle constraints.

(7) Thermal unit output constraints

$$P_{g,t}^{0} + R_{g,t}^{+} \leq P_{g,\max} u_{g,t} \tag{21}$$

$$P_{g,t}^{0} - R_{g,t}^{-} \geq P_{g,\min} u_{g,t} \tag{22}$$

(8) Thermal unit creep constraints

When the minimum output $P_{\min}$ for thermal unit g to start surpassing the climb rate, the conventional unit climb constraints will prevent all shutdown units from starting. Given this mechanism, therefore, the following improvement is established:

$$\left(P_{g,t}^{0}+R_{g,t}^{+}\right)-\left(P_{g,t-1}^{0}-R_{g,t-1}^{-}\right)\le u_{g,t-1}\left(R_{U,g}-\frac{P_{g,\max}+P_{g,\min}}{2}\right)+\frac{P_{g,\max}+P_{g,\min}}{2} \tag{23}$$

$$\left(P_{g,t-1}^{0}+R_{g,t-1}^{+}\right)-\left(P_{g,t}^{0}-R_{g,t}^{-}\right)\le u_{g,t}\left(R_{D,g}-\frac{P_{g,\max}+P_{g,\min}}{2}\right)+\frac{P_{g,\max}+P_{g,\min}}{2} \tag{24}$$

where $R_{U,g}$ and $R_{D,g}$ indicate the maximum values of thermal unit g climbing up and down, respectively.

(9) Thermal unit reserve capacity constraints

$$0\le R_{g,t}^{+}\le R_{g,t,\max}^{+} \tag{25}$$

$$0\le R_{g,t}^{-}\le R_{g,t,\max}^{-} \tag{26}$$

$$\sum_{g\in N_G}R_{g,t}^{+}\ge R_{t,\min}^{+} \tag{27}$$

$$\sum_{g\in N_G}R_{g,t}^{-}\ge R_{t,\min}^{-} \tag{28}$$

where $R_{g,t,\max}^{+}$ and $R_{g,t,\max}^{-}$ represent the upper limit values of upward and downward reserve capacity that can be provided by thermal power unit g from the day-ahead phase to the intra-day phase at time t. $R_{t,\min}^{+}$ and $R_{t,\min}^{-}$ refer to the minimum total upward reserve capacity and the minimum total downward reserve capacity required by the system at time t, respectively.

(10) Wind farm, photovoltaic station output constraints

$$0\le P_{\omega,t}^{0}\le A_{\omega,t}^{0} \tag{29}$$

$$0\le P_{v,t}^{0}\le A_{v,t}^{0} \tag{30}$$

(11) Pumped storage unit capacity, reservoir capacity, operating condition constraints

$$e_{\min}\le e_{i,t}^{0}\le e_{\max} \tag{31}$$

$$p_{\min}\le p_{i,t}^{0}\le p_{\max} \tag{32}$$

where $e_{\min}$ and $e_{\max}$ symbolize the minimum and maximum outputs of pumped storage unit i under generation conditions; $p_{\min}$ and $p_{\max}$ denote the minimum and maximum outputs of pumped storage unit i under pumping conditions, respectively.

$$V_{\min}\le V_t\le V_{\max} \tag{33}$$

$$V_t=V_{t-1}-\beta e_{i,t}^{0}T_0+\eta p_{i,t}^{0}T_0 \tag{34}$$

$$V_{st}=V_{end} \tag{35}$$

where V_t stands for the reservoir capacity at the moment of t; $V_{\min}$ and $V_{\max}$ are defined as the minimum and maximum reservoir capacity, respectively; T_0 is specified as the length of the scheduling period; β and η are expressed as the efficiency of pumped storage unit power generation and pumping cycle, respectively; V_{st} and V_{end} signify the beginning and end of the scheduling cycle reservoir capacity, respectively. Eq. (33) refers to the upper/lower limit constraint of reservoir capacity, Eq. (34) formulates the constraint of the relationship between reservoir capacity in neighboring periods, and Eq. (35) describes the constraint of the beginning and end reservoir capacity.

$$y_{e,t} + y_{p,t} \le 1 \tag{36}$$

$$y_{e,t} + y_{p,t+1} \le 1 \tag{37}$$

$$y_{e,t+1} + y_{p,t} \le 1 \tag{38}$$

where the pumped storage unit cannot run in the power generation condition and pumping condition simultaneously, and the two conditions cannot be directly switched due to a downtime buffer time as the requisite.

3.2. Intraday phase adjustment

(1) Objective function

$$\begin{aligned} \max_{U} \min C_{sub} = & \sum_{t=1}^{N_T} \sum_{g=1}^{N_G} \left(C_g^{s,R+} \Delta P_{g,t}^{s+} + C_g^{s,R-} \Delta P_{g,t}^{s-} \right) \\ & + \sum_{t=1}^{T_{e,t}} \sum_{i=1}^{N_H} F_{e,t}(\Delta e_{i,t}^{s}) y_{e,i,t} - \sum_{t=1}^{T_{p,t}} \sum_{i=1}^{N_H} F_{p,t}(\Delta p_{i,t}^{s}) y_{p,i,t} \\ & + C^{\omega,cur} \sum_{\omega=1}^{N_\omega} \left(A_{\omega,t}^{s} - P_{\omega,t}^{s} \right) + C^{v,cur} \sum_{v=1}^{N_v} \left(A_{v,t}^{s} - P_{v,t}^{s} \right) \end{aligned} \tag{39}$$

where $C_g^{s,R+}$ and $C_g^{s,R-}$ are defined as the upward and downward reserve costs for thermal power units in the intraday stage, respectively; $\Delta P_{g,t}^{s+}$ and $\Delta P_{g,t}^{s-}$ indicate the upward and downward reserve quantities for thermal power units, respectively; $\Delta e_{i,t}^{s}$ and $\Delta p_{i,t}^{s}$ represent the generating power and pumping power for pumped storage units in the intraday stage, respectively; $P_{\omega,t}^{s}$ and $P_{v,t}^{s}$ denote the consumption quantities of wind farms ω and photovoltaic stations v in the intraday stage, respectively; $C^{\omega,cur}$ and $C^{v,cur}$ stand for the costs of penalizing the abandonment of wind and photovoltaic.

(2) Power balance constraints

$$\sum_{g \in G_b} P_{g,t}^{s} + \sum_{\omega \in W_b} P_{\omega,t}^{s} + \sum_{v \in V_b} P_{v,t}^{s} + \sum_{i \in I_b} \Delta e_{i,t}^{s} - \sum_{i \in I_b} \Delta p_{i,t}^{s} - L_{b,t} = \sum_{l:o_2(l)=b} P_{l,t}^{s} - \sum_{l:o_1(l)=b} P_{l,t}^{s} \tag{40}$$

(3) Wind and photovoltaic output constraints

$$0 \le P_{\omega,t}^{s} \le A_{\omega,t}^{s} \tag{41}$$

$$0 \le P_{v,t}^{s} \le A_{v,t}^{s} \tag{42}$$

(4) Calling on thermal unit reserve constraints

$$P_{g,t}^{s} = P_{g,t}^{0} + \Delta P_{g,t}^{s+} - \Delta P_{g,t}^{s-} \tag{43}$$

$$0 \le \Delta P_{g,t}^{s+} \le R_{g,t}^{+} \tag{44}$$

$$0 \le \Delta P_{g,t}^{s-} \le R_{g,t}^{-} \tag{45}$$

(5) Calling on thermal unit reserve constraints

$$0 \le \Delta e_{i,t}^{s} \le e_{i,t}^{0} \tag{46}$$

$$0 \le \Delta p_{i,t}^{s} \le p_{i,t}^{0} \tag{47}$$

(6) Line currents and safety constraints

In the risky operation scenario, to eliminate the tripping of the line, which is caused by the transmission line failure and ensuing current shifting of the grid, the power on the transmission line in the grid is required to satisfy the formula below:

$$-M_1 z_l \le P_{l,t}^s - \frac{\theta_{o_1(l),t}^s - \theta_{o_2(l),t}^s}{x_l} \le M_1 z_l \tag{48}$$

$$-P_l^{\max}\left(1-Z_l\right) \le P_{l,t}^s \le P_l^{\max}\left(1-Z_l\right) \tag{49}$$

where M_1 is a sufficiently large constant, adopted as $P_l^{\max} + \left(\overline{\theta} - \underline{\theta}\right)/x_l$; Z_l is denoted as whether the line is out of service with a fault, expressed as a 0-1 integer variable.

$$\overline{\theta} \le \theta_{b,t}^s \le \underline{\theta} \tag{50}$$

$$\theta_{\mathrm{ref},t}^s = 0 \tag{51}$$

4. Model Solution

This paper presents a min-max-min three-layer optimization model. Established solution methodologies encompass Bender's decomposition and Column and Constraint Generation (C&CG). These algorithms decompose the original problem into a master problem and subproblems. The two-layer optimization subproblems are subsequently streamlined into single-layer optimization tasks, leveraging the Karush-Kuhn-Tucker (KKT) conditions or the Strong Duality Theory (SDT). By employing the SDT, the two-layer optimization subproblem is transformed into a single-layer optimization problem, thereby facilitating the iterative resolution of the master-subproblem structure to attain the optimal solution for the original problem.

Of the available methods, the C&CG algorithm using Primal Cutting Plane to return to the master problem demonstrates superior efficiency compared to the Benders decomposition approach employing dual cutting plane returns. Thus, this study opts for the C&CG algorithm to tackle the two-stage, three-layer optimization problem. Applying SDT to resolve the two-layer max-min optimization subproblem ensures alignment in the solution direction. Specifically, the inner minimization problem is converted into a maximization problem, maintaining coherence within the solution framework of the model.

$$\min_{x^0 \in \Omega^0} (c^0)^T x^0 + \min_{z \in U}\left(b_0^T u_\omega + b_1^T u_v + \min_{x^s \in \Omega^s} (c^s)^T x^s\right) \tag{52}$$

$$\Omega^0 = \left\{x^0 \middle| Ax^0 \le a\right\} \tag{53}$$

$$U = \left\{ z \middle| \begin{array}{l} u_\omega = u_\omega^0 + \Delta U_\omega^+ Z_\omega^+ + \Delta U_\omega^- Z_\omega^-, u_v^0 + \Delta U_v^+ Z_v^+ + \Delta U_v^- Z_v^-, \\ B_\omega\left(Z_\omega^+ + Z_\omega^-\right) \le \Gamma_\omega, B_v\left(Z_v^+ + Z_v^-\right) \le \Gamma_v, B_l Z_l \le \Gamma_l \end{array} \right\} \tag{54}$$

$$\Omega^s = \left\{x^s \middle| Dx^s \le Ex^0 + F_0 u_\omega^0 + F_1 u_v^0 + Gz + d\right\} \tag{55}$$

where x^0 signifies the day-ahead phase control variable, including $P_{g,t}^0$, $R_{g,t}^+$, $R_{g,t}^-$, $u_{g,t}$, $P_{\omega,t}^0$, $P_{v,t}^0$, $P_{l,t}^0$, $\theta_{b,t}^0$, $e_{i,t}^0$, and $p_{i,t}^0$; x^s symbolizes the intraday phase control variable, including $\Delta P_{g,t}^{s+}$, $\Delta P_{g,t}^{s-}$, $P_{\omega,t}^s$, $P_{v,t}^s$, $\theta_{b,t}^s$, and $P_{l,t}^s$; u_ω^0 and u_ω denote the available wind power in the day-ahead and intraday phases, respectively; u_v^0 and u_v are specified as the available photovoltaic power in the day-ahead and intraday phases, respectively; $z = (Z_\omega^+, Z_\omega^-, Z_v^+, Z_v^-, z_l)$ means an integer variable of 0-1 to denote the uncertainty of wind power (Z_ω^+, Z_ω^-), the uncertainty of photovoltaic power (Z_v^+, Z_v^-), and the outage of the transmission line failure (z_l).

Eq. (52) depicts the objective function of the day-ahead-intraday two-phase model; Eq. (53) represents the day-ahead constraints including constraints Eqs. (9)-(38); Eq. (54) explicates the set of risky operating scenarios including Eqs. (1)-(6); Eq. (55) delineates the intraday phase constraints including Eqs. (40)-(51). c^0, b_0, b_1, c^s, A, a, ΔU_ω^+, ΔU_ω^-, ΔU_v^+, ΔU_v^-, B_ω, B_v, B_l, Γ_ω, Γ_v, Γ_l, D, E, F_0, F_1, G, and d are the constants matrices corresponding to the objective function and the constraints.

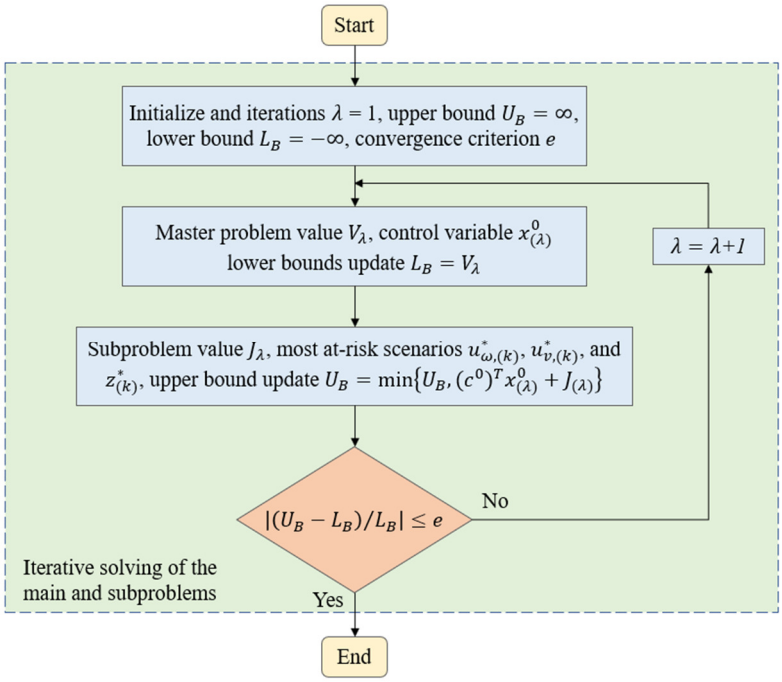

Fig. 3 Flowchart of C&CG algorithm

The master problem includes the day-ahead stage model and sub-problems to find the riskiest operating condition constraints, and the master problem during the λth iteration is shown in:

$$\min\left((c^0)^T x^0 + \eta\right) \tag{56}$$

$$\text{s.t.} = \begin{cases} Ax^0 \le a \\ \eta \ge b_0^T u^*_{\omega,(k)} + b_1^T u^*_{v,(k)} + (c^s)^T x^s_{(k)}, \ 0 \le k \le \lambda - 1 \\ Dx^s_{(k)} \le Ex^0 + F_0 u^0_\omega + F_1 u^0_v + Gz^*_{(k)} + d, \ 0 \le k \le \lambda - 1 \end{cases} \tag{57}$$

where $u^*_{\omega,(k)}$, $u^*_{v,(k)}$, and $z^*_{(k)}$ are defined as the riskiest operating conditions solved by the subproblems; $x^*_{(k)}$ is designated to be the new optimization variable for the master problem; η is expressed to be the value of the objective function for the intraday phase to be optimized.

The subproblem is a two-layer max-min optimization problem, and the inner minimization problem is transformed into a maximization problem utilizing pairwise solid theory, and the transformed λth iteration subproblem is modeled as follows:

$$\max\left[b_0^T u_\omega + b_1^T u_v + \left(Ex^0_{(\lambda)} + F_0 u^0_\omega + F_1 u^0_v + Gz + d\right)\sigma\right] \tag{58}$$

$$\text{s.t.} = \begin{cases} D^T \sigma \le c^0 \\ \sigma \le 0 \\ z \in U \end{cases} \tag{59}$$

where σ is the dyadic variable for the intraday phase constraints.

The transformed model contains the bilinear term $z^T\sigma$, since z is a state 0-1 variable, and this bilinear term can be strictly linearized by introducing the variable θ using the large M method, as shown in:

$$\theta \ge -M_2 z \tag{60}$$

$$\theta \ge \sigma \tag{61}$$

$$\theta \le \sigma - M_2(z-1) \tag{62}$$

$$\theta \le 0 \tag{63}$$

where M_2 is a constant variable that takes the value of infinity. The steps of the algorithm are specifically shown in Fig. 3, which shows the flowchart of the C&CG algorithm.

5. Example Analysis

In this paper, the improved IEEE 14-node and 30-node systems are selected as the research objects to build the active prevention and control model in grid cascading tripping and carry out the analysis of day-ahead and intra-day optimal scheduling, as shown in Figs. 4-5.

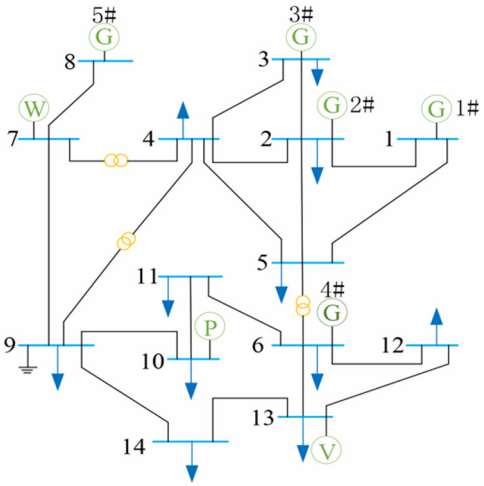

Fig. 4 IEEE14 node system connection diagram

Note: "P" for pumped storage units; "W" for wind units; "V" for photovoltaic units; "G" for thermal units

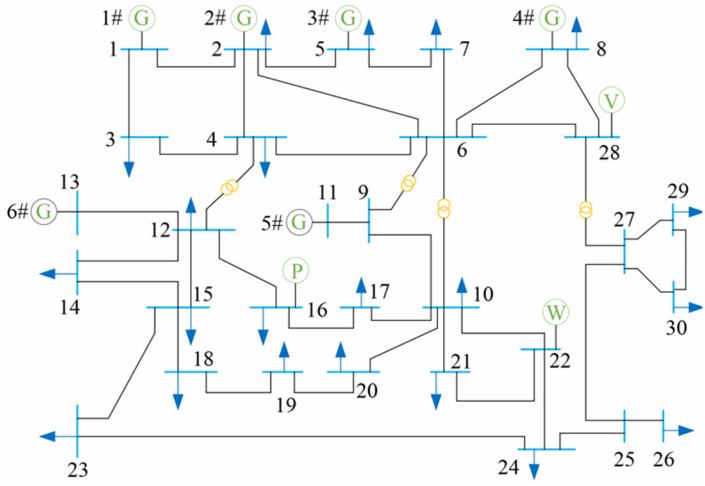

Fig. 5 IEEE30 node system connection diagram

Note: "P" for pumped storage units; "W" for wind units; "V" for photovoltaic units; "G" for thermal units

The period of daily load data optimization scheduling is 24h, with 1h as the time division scale. The installed capacity of the pumped storage is 80 MW, the conversion efficiency under generation and pumping conditions is β = 0.9 and η = 0.85, respectively [18], the maximum capacity of the upper and lower reservoirs stands at $V_{\max}$ = 350 MW, the minimum capacity of the upper and lower reservoirs is $V_{\min}$ = 50 MW, and the beginning and end capacity of the upper and lower reservoirs accounts $V_{st} = V_{end}$ = 200 MW and the generation and pumping costs for the day-ahead stage consume \$100/(MWh) and \$80/(MWh), respectively, and the intra-day costs for the day-ahead and intra-day adjustment stages are taken to be \$100/(MWh) and \$80/(MWh), respectively.

The node system load forecast is shown in Table 1. The generation and pumping costs for the adjustment phase are taken as \$5/(MWh). The system is equipped with a wind farm with a total capacity of 350 MW and a photovoltaic station of 60 MW, and the penalty cost of wind and photovoltaic abandonment, which is for the wind farm ω and the photovoltaic station v in the intraday phase, is taken as $C^{\omega,cur} = C^{v,cur}$ = \$20/(MWh), and the schematic diagrams of the fluctuating region of wind and photovoltaic output are presented in Figs. 6 and 7 to characterize the uncertainty of the wind and photovoltaic output [19]. The coal consumption factor, climb rate, and output power of thermal units are shown in Table 2 (using the IEEE30 node as an example), the nonlinear fuel cost function of the unit is divided into m_0 = 20 segments, the unit up and down reserve capacity stands at 20 MW, the unit up and down reserve cost for the day-ahead phase is taken as \$40/(MWh), and the unit up and down reserve cost for the day-ahead adjustment phase accounts for \$5/(MWh).

Table 1 IEEE30 node system load forecasts

Time	1	2	3	4	5	6	7	8	9	10	11	12
Prediction	351.2	342.8	336.5	334.5	334.5	399.5	438.9	464.1	482.9	485.1	485.7	482.9
Time	13	14	15	16	17	18	19	20	21	22	23	24
Prediction	482.9	482.9	478.7	480.8	490.9	493.4	493.4	479.1	401.4	384.7	362.8	361.8

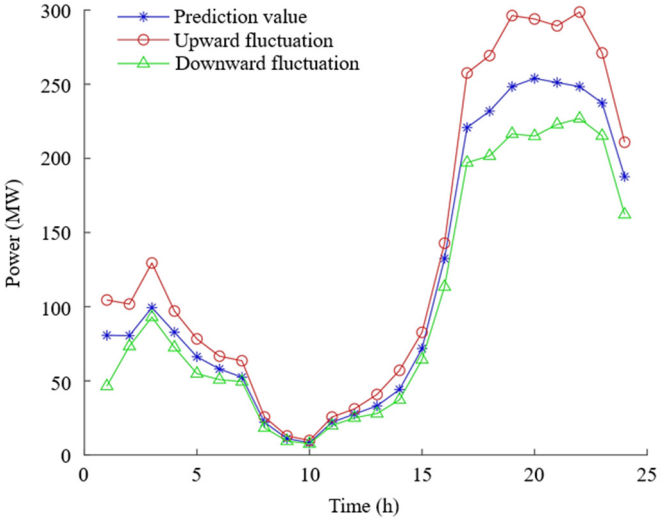

Fig. 6 Wind forecasts and fluctuations

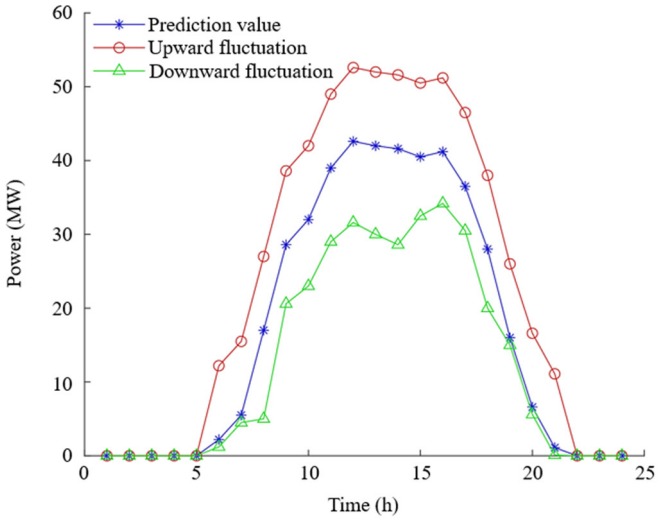

Fig. 7 Photovoltaic forecasts and fluctuations

Table 2 IEEE30 node system main parameters of thermal power units

Unit	$P_{g,\max}$ (MW)	$P_{g,\min}$ (MW)	a_g ($/MW^{2}h)	b_g ($/MW)	c_g ($/h)	$R_{U,g}/R_{D,g}$ (MW/h)
1#	157.49	50	0.1524	38.5397	786.7988	37.5
2#	100	25	0.1058	46.1591	945.6332	30
3#	60	15	0.028	40.3965	1049.998	15
4#	80	20	0.0354	38.3055	1243.531	20
5#	40	10	0.0211	26.3278	1258.57	15
6#	40	10	0.0179	28.2704	1156.659	15

5.1. Risk scenario selection

This subsection analyzes two severe scenarios pertinent to wind-photovoltaic uncertainty and line fault outage. In selecting transmission line fault outages within risky scenarios, this paper presents a selection of outcomes across multifarious systems, as delineated in Table 3, and contrasts them with existing methodologies [20]. As evident from Table 3, the critical lines identified predominantly cluster between generators and loads.

Table 3 Critical line identification for different node systems

Critical line	IEEE14 node system		Critical line	IEEE30 node system	
	Electric betweenness/Rank	Literatures [20]/Rank		Electric betweenness/Rank	Literatures [20]/Rank
1-2	509 610/1	5/7	1-2	1 441 000/1	14/11
4-5	419 430/2	5/8	6-8	1 362 600/2	4/28
2-4	133 660/3	10/4	4-6	1 029 900/3	11/13
2-5	117 170/4	4/12	21-22	897 890/4	24/4
2-3	100 720/5	1/18	3-4	877 760/5	13/12
9-10	84 939/6	5/9	6-7	499 740/6	4/27

This observation underscores that these lines bear heavier power loads despite their peripheral positioning within the system. The proposed electric betweenness integrates power and load locations, reflecting network structural characteristics. This approach diverges from merely considering the overarching system structure, emphasizing line interdependencies within the system topology. In addressing the risky scenario of wind-photovoltaic output uncertainty, which employs a framework that incorporates uncertainty sets denoted as $\prod_{\omega}$ = 24 for wind power and $\prod_{v}$ = 24 for photovoltaic power, the two-stage system model endeavors to identify the most precarious wind-photovoltaic fluctuation scenarios, as depicted in Figs. 8-9. Subsequently, this model facilitates the simulation of these risky scenarios to inform unit reserve protocols and pumped storage adjustments.

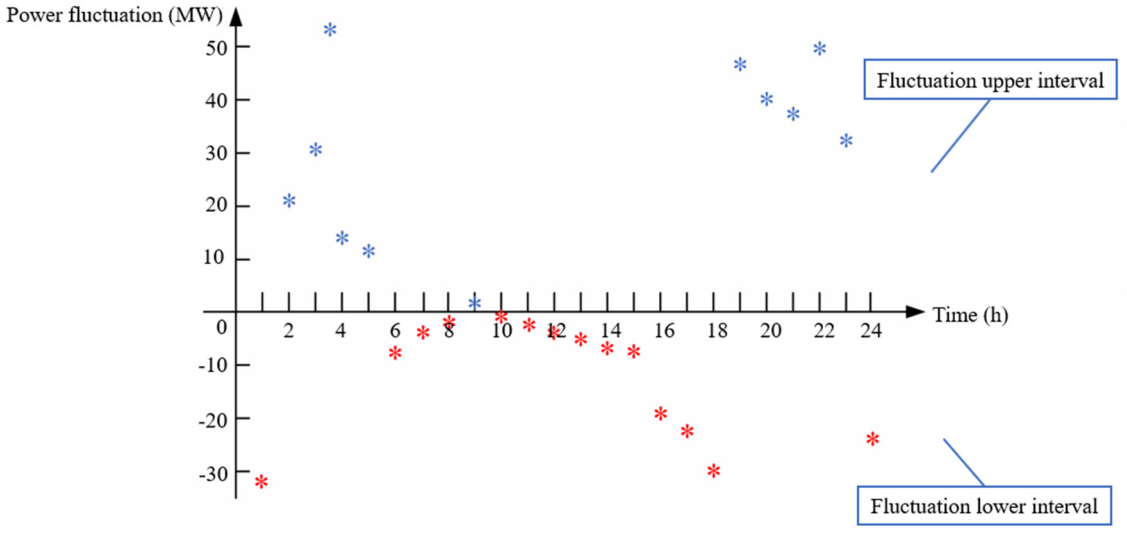

Fig. 8 Wind power fluctuation range

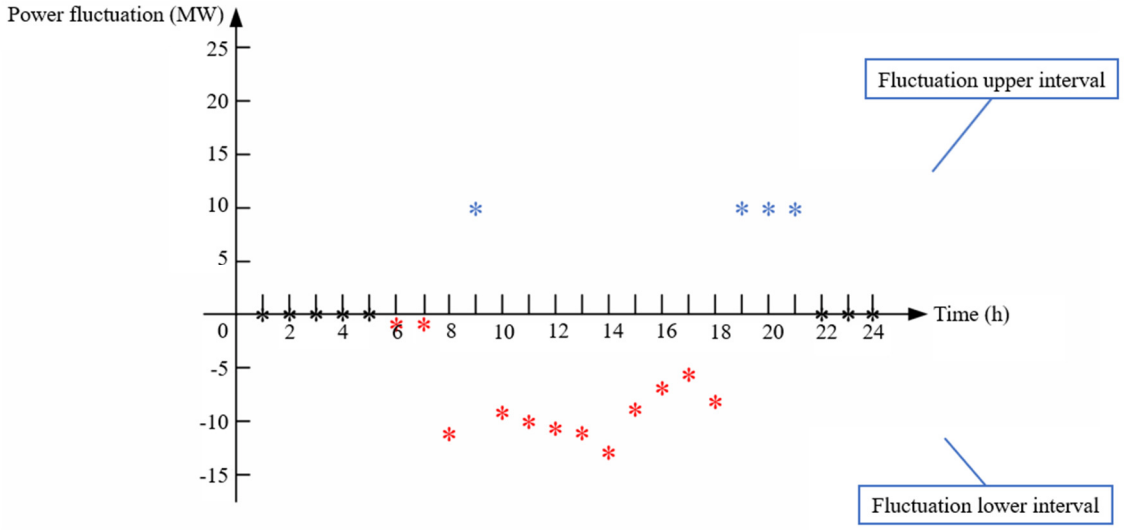

Fig. 9 Photovoltaic fluctuation range

5.2. *Analysis of the results of risky operational scenarios*

Based on the study of risk scenarios, this paper focuses on the IEEE30 node system as its primary subject of study. The IEEE30 node system thoroughly examines the ramifications of wind-photovoltaic power uncertainties and the consequences of critical transmission line failures on the grid. The optimization outcomes for four distinct operational scenarios are meticulously detailed in Table 4 which delineates the scheduling intricacies and operational costs associated with each scenario under its most precarious conditions.

Scenario 1: Regular day-ahead scheduling mode without considering renewable energy uncertainty and critical line failure outages.

Scenario 2: Considering only the uncertainty of the renewable energy, the uncertainty set $\prod_{\omega}$ for wind power is set to 24, and the uncertainty set $\prod_{v}$ for photovoltaic is set to 12.

Scenario 3: Considering only the critical line failure outage, according to Table 3, set the outage line as branches 1-2.

Scenario 4: Renewable energy uncertainty and critical line failure outages are simultaneously considered.

Table 4 illustrates a noteworthy trend: the total system dispatch cost escalates with the complexity of risk scenarios. This escalation is primarily attributed to the imperative of mitigating the ramifications stemming from the variability of renewable energy sources and potential line failures. Notably, Scenario 1 serves as an instrumental benchmark against the other three

scenarios, where the absence of unit operation cost elucidates a significant insight, i.e., the reserve capacity of thermal power units remains largely dormant in conventional dispatch paradigms. However, when confronted with risk scenarios characterized by wind-photovoltaic uncertainty and line failure-induced shutdowns, the coordinated utilization of unit reserve capacity alongside pumped storage units. Meanwhile, a tangible reduction is manifested in overall system dispatch costs as the pumped storage units concurrently bolster system stability.

Table 4 Optimization results considering different factors

Scenario	Unit operating cost ($)	Unit reserve cost ($)	Pumped storage cost ($)		Total scheduling cost ($)
			Generating	Pumping	
1	445 560	0	32 738	34 131	444 210
2	450 410	7 919	24 784	27 394	468 260
3	471 550	24 048	20 289	21 049	510 360
4	469 460	25 374	29 594	28 900	522 620

Figs. 10-11 corroborate the importance of pumped storage units in facilitating peak shaving and valley filling operations. These operations and the strategic deployment of unit reserve output effectively address the exigencies posed by risky and intricate scenarios. Comparative analysis reveals that in scenarios solely involving line failures and shutdowns, integrating thermal power unit reserve capacity translates into a commendable cost saving of $2090. Such a cost-saving ensures the efficient and stable operation of thermal power units and safeguards the utilization rate of clean energy sources. Considering all aforementioned aspects, adopting a scheduling scheme encompassing multiple factors inevitably entails heightened costs in day-ahead base state scheduling. Nevertheless, this approach substantially fortifies the resilience of the system against risks, thus corroborating the efficacy of a two-stage system paradigm.

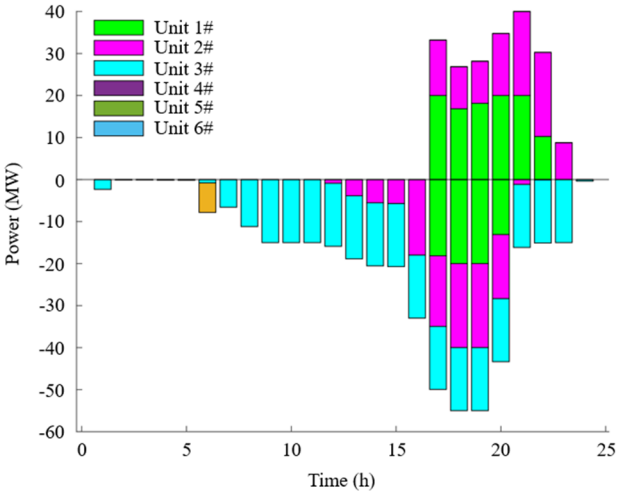

Fig. 10 Scenario 4 reserve output

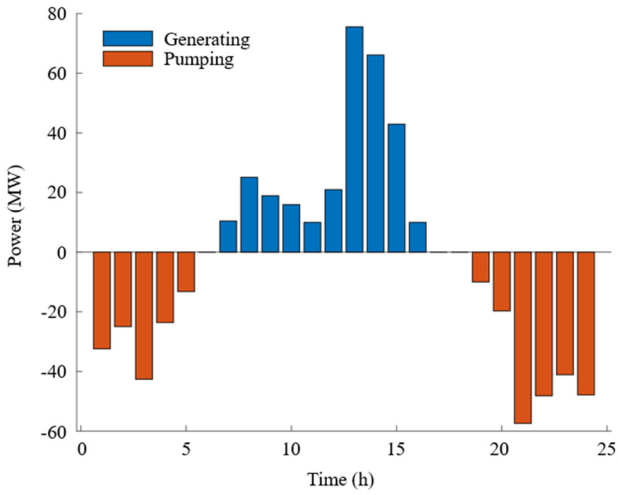

Fig. 11 Scenario 4 pumped storage output

5.3. *Effectiveness of pumped storage*

To further illustrate the role of pumped storage in enhancing the stability and flexibility of the system operation, this section analyzes the performance of model 2 by presenting the model operation based on risk scenario 4, as shown in Table 5.

Model 1: No pumped storage added to the regulation.

Model 2: With pumped storage involved in regulation.

Table 5 Model optimization results before and after pumped storage implementation

Model	Total cost ($)	Unit cost ($)	Total unit start-up time (h)	Renewable energy abandonment rate (%)	Standard deviation of output (MW)
1	544 370	480 570	113	7.34	90.87
2	522 620	469 460	100	0.65	74.13

Comparing the outcomes derived from Model 1 and Model 2, it is evident that integrating pumped storage facilities for system regulation yields a noteworthy reduction in total regulation costs by $21,750. Moreover, a marked enhancement emerges in the overall performance of thermal power units concerning total start-up time and associated costs, in contrast to scenarios where pumped storage integration is absent from the grid. Notably, the standard deviation of output from thermal power units has been decreased from the initial 90.87 MW to 74.13 MW, thereby facilitating efficient and seamless operation of thermal power with pumped storage facilities.

Compare with Fig. 12(a), this assertion is supported by the findings illustrated in Fig. 12(b), which demonstrate that during the time intervals of 9-15, a surge is manifested in electricity consumption, coinciding with pumped storage operations in the power generation mode. Consequently, the demand for thermal power units is alleviated, ensuring surplus capacity within the system to accommodate renewable energy sources while satisfying supply requirements. Conversely, during the intervals of 19-24, characterized by low-demand states and significant contributions of wind power to the grid, pumped storage units operated in pumping mode. As a result, the rate of new energy abandonment is mitigated, reducing it from the initial 7.34% to 0.65%. The proposed pumped storage scheduling strategy effectively mitigates the adverse impacts of integrating renewable energy sources on system operations, thereby preserving the efficient and stable operation of thermal power units, ultimately ensuring the promotion of clean energy consumption within the system.

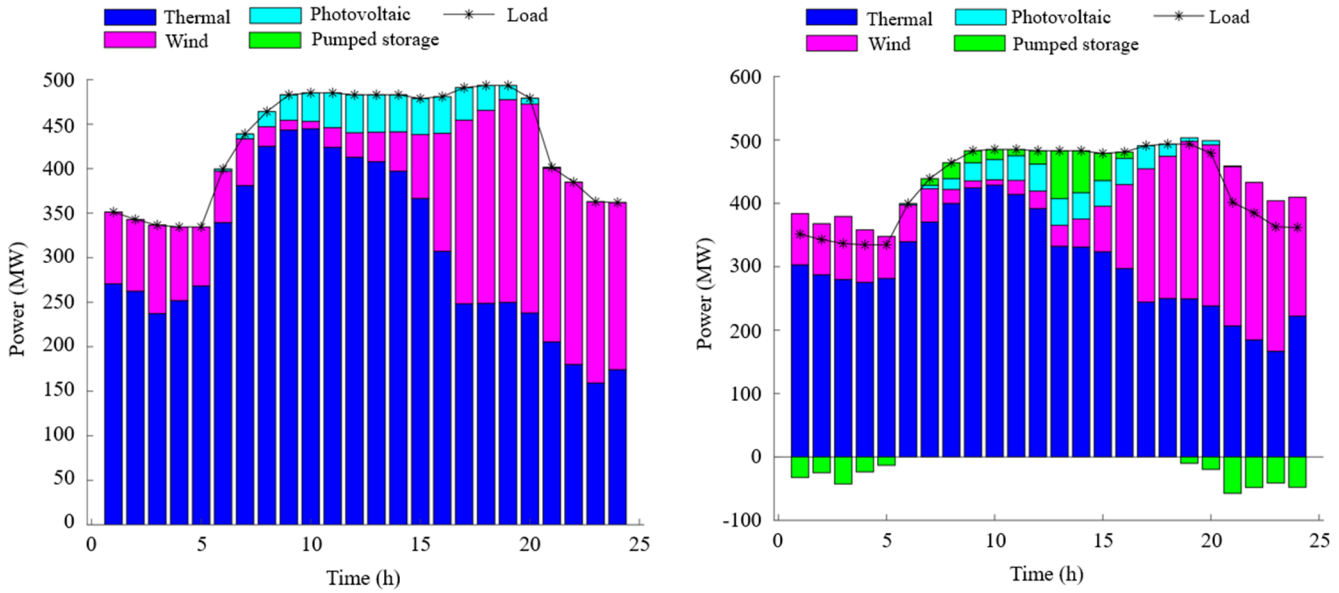

(a) No pumped storage participation (b) Pumped storage participation

Fig. 12 Two-stage system optimization scheduling results

5.4. Line outage safety analysis

Considering the trend propagation characteristics of the power system, line failure outages can precipitate a cascade effect, leading to the cessation of additional lines and ensuing occurrence exacerbation of chain faults. To elucidate the efficacy of the proposed model in averting chain failures, this section employs line transmission capacity metrics to delineate the carrying capacity of individual lines within different system sectors after delisting. Specifically, critical lines 6-8, 4-6, 21-22, and 3-4 are scrutinized to analyze alterations in transmission dynamics over a daily cycle under the two-stage model, as depicted in Fig. 13. The repercussions of line outages are portrayed on the transmission capacity of interconnected lines, along with fluctuations in their carrying capacity.

Notably, Fig. 13(d) illustrates a notable increase in power transmission through lines 3-4, attributable to its proximity to units #1 and #2 and its role in mitigating the tidal shifts following the failure outage of lines 1-2. Conversely, in Fig. 13(c), the power transmitted via lines 21-22 exhibits marginal variation, with a subsequent decrease during the latter half of the dispatch

period. This phenomenon is attributed to pronounced fluctuations in the wind during this timeframe, necessitating the redistribution of transmission stress to alternative lines. All pivotal transmission lines operated within their prescribed tolerances, with system dispatch being harmonized with the pumped storage infrastructure to mitigate losses arising from precarious scenarios. This underscores the validation of the proposed research model within this study context.

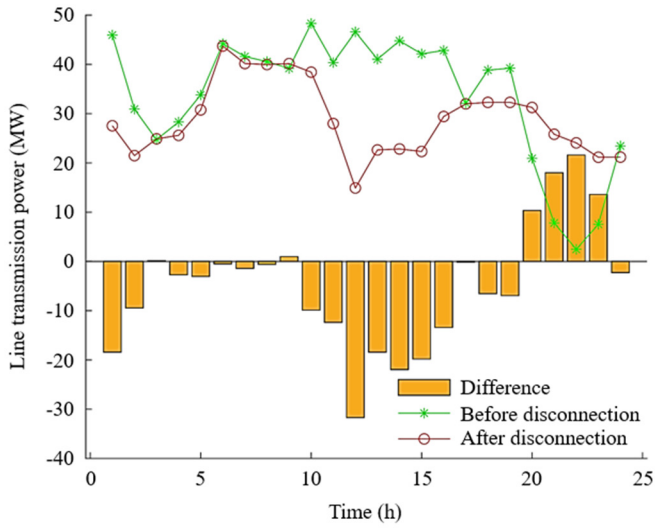

(a) Line 6-8

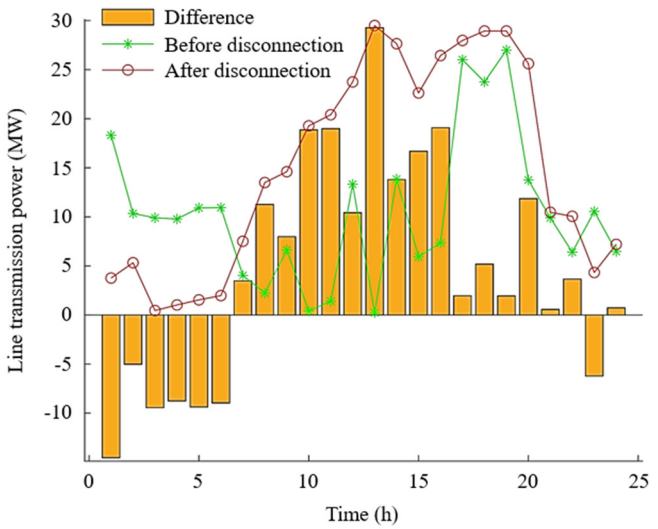

(b) Line 4-6

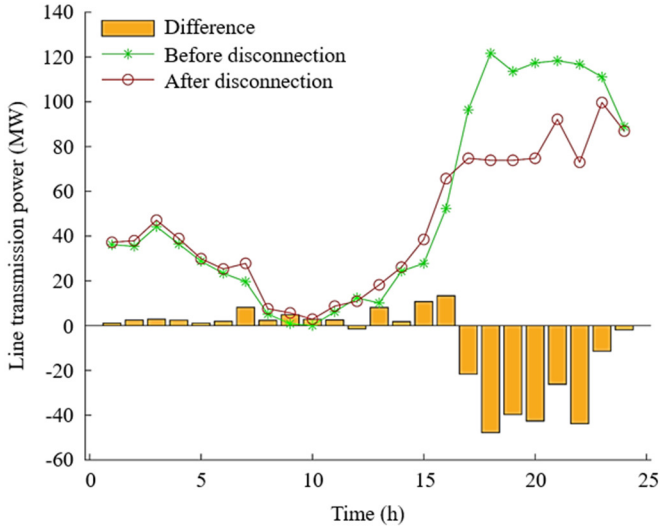

(c) Line 21-22

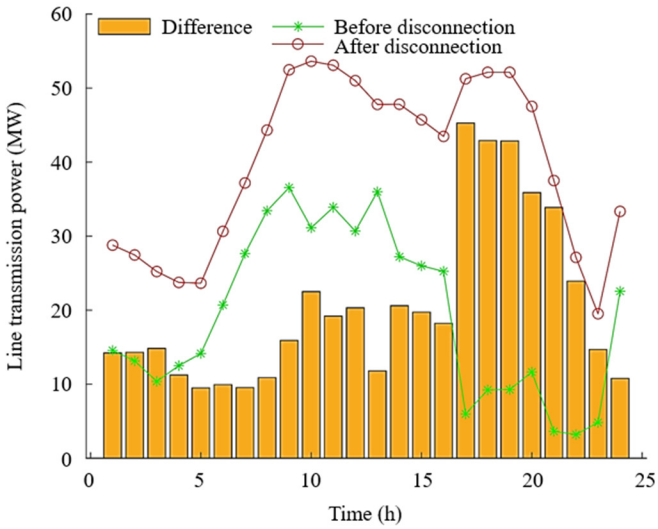

(d) Line 3-4

Fig. 13 Carrying capacity of critical lines

6. Conclusions

This study presents an active prevention and control against the power grid, considering tripping and pumped storage integration. The proposed approach aims to bolster system operational flexibility by synergizing two regulation mechanisms: conventional unit reserve and pumped storage utilization. Moreover, the optimization framework adopts a two-stage approach encompassing day-ahead planning and intra-day adjustments, accommodating the uncertainties associated with fluctuating outputs from renewable sources, especially wind and photovoltaic energy. The ensuing deductions drawn from the computational analysis are summarized as follows:

(1) The risk scenarios comprehensively incorporate the uncertainties associated with wind–photovoltaic output and potential transmission line failures and shutdowns. The approach to identifying critical lines during failure events employs an electric betweenness method, which effectively captures the practice of each transmission line by individual "generation-load" nodes. The physical underpinnings align more closely with the inherent characteristics of power

systems, enabling consideration of varying generation capacities and load levels. Apropos innovation in addressing uncertainties in renewable energy output, the temporal and spatial uncertainty sets can be adjusted to equalize economic efficiency and system stability.

(2) Combining unit reserve and rapid response from pumped storage facilities can significantly enhance system flexibility. While unit reserve renders direct control over thermal power output, thereby bolstering system stability and yielding more reductions in costs, the peak shaving and valley filling capabilities of pumped storage units alleviate the strain on thermal power units during periods of high demand. Additionally, integrating clean energy sources is facilitated, thus mitigating fluctuations in renewable energy generation fed into the grid. System operational efficiency is substantially enhanced by synergistically optimizing the responses of both unit types. This coordinated approach to unit response yields significant improvements in overall system performance.

This model is deployed to minimize the total operating cost of the system while operating under the most precarious conditions posed by intraday scenarios. Notably, alongside considerations of system economics, the model also addresses the issue of chain failures arising from trend shifts after line fault shutdowns. By incorporating the aforementioned factors into the optimization framework, a comprehensive system operation and risk management analysis is consummated.

Acknowledgments

This research was financially supported by the Fujian Natural Science Foundation Project under the grant 2022J01948, and the Scientific Research Development Foundation of Fujian University of Technology under the grant GY-Z17149.

Conflicts of Interest

The authors declare no conflict of interest.

References

[1] P. Ju, T. Y. Jiang, and Y. Huang, “Brief Discussion on the “Three-Self” Nature of the New Power System,” Proceedings of the CSEE, vol. 43, no.7, pp. 2598-2608, 2023. (In Chinese)

[2] G. Yu, T. Hao, and J. X. Zhu, “Discussion on Action Strategies of China’s Carbon Peak and Carbon Neutrality,” Bulletin of Chinese Academy of Sciences, vol. 37, no. 4, pp. 423-434, 2022.

[3] Z. Zhang and C. Kang, “Challenges and Prospects for Constructing the New-Type Power System towards a Carbon Neutrality Future,” Proceedings of the CSEE, vol. 42, no. 8, pp. 2806-2819, 2022. (In Chinese)

[4] Y. Jiang, Z. Ren, Q. Li, Y. Guo, and Y. Xu, “An Accommodation Strategy for Renewable Energy in Distribution Network considering Coordinated Dispatching of Multi-Flexible Resources,” Transactions of China Electrotechnical Society, vol. 37, no. 7, pp. 1820-1835, 2022.

[5] T. Li, W. Hu, J. Li, X. Han, and Z. Chen, “Intelligent Economic Dispatch for PV-PHS Integrated System: A Deep Reinforcement Learning-Based Approach,” Transactions of China Electrotechnical Society, vol. 35, no. 13, pp. 2757-2768, 2020.

[6] Z. Cao, H. Chen, P. Hu, and L. Chen, “Day-ahead and Intraday Two-Stage Optimal Dispatch Model of a Thermal Power Plant Withenergy Storage and Taking into Account the Profit,” Power System Protection and Control, vol. 49, no. 12, pp. 106-113, 2021. (In Chinese)

[7] Z. Zhang, W. Wang, X. Ma, X. Zhang, Y. Chu, K. Wang, et al., “Reserve of Power System Considering Renewable Energy Based on Risk Control,” Journal Power System Technology, vol. 44, no. 9, pp. 3375-3382, 2020. (In Chinese)

[8] P. Li, D. Yu, M. Yang, and J. Wang, “Flexible Look-Ahead Dispatch Realized by Robust Optimization considering CVaR of Wind Power,” IEEE Transactions on Power Systems, vol. 33, no. 5, pp. 5330-5340, September 2018.

[9] Y. Lin, Y. Ding, Y. Song, and C. Guo, “A Multi-State Model for Exploiting the Reserve Capability of Wind Power,” IEEE Transactions on Power Systems, vol. 33 no. 3, pp. 3358-3372, May 2018.

[10] F. J. Heredia, M. D. Cuadrado, and C. Corchero, “On Optimal Participation in the Electricity Markets of Wind Power Plants with Battery Energy Storage Systems,” Computers & Operations Research, vol. 96, pp. 316-329, August 2018.

[11] T. Aziz, N. A. Masood, S. R. Deeba, W. Tushar, and C. Yuen, "A Methodology to Prevent Cascading Contingencies Using BESS in A Renewable Integrated Microgrid," International Journal of Electrical Power & Energy Systems, vol. 110, pp. 737-746, September 2019.

[12] M. Z. Zakariya and J. Teh, "A Systematic Review on Cascading Failures Models in Renewable Power Systems with Dynamics Perspective and Protections Modeling," Electric Power Systems Research, vol. 214, Part B, article no. 108928, January 2023.

[13] H. Geramifar, M. Shahabi, and T. Barforoshi, "Coordination of Energy Storage Systems and DR Resources for Optimal Scheduling of Microgrids under Uncertainties," IET Renewable Power Generation, vol. 11, no. 2, pp. 378-388, February 2017.

[14] K. D. Pippi, T. A. Papadopoulos, and G. C. Kryonidis, "Impact Assessment Framework of PV-BES Systems to Active Distribution Networks," IET Renewable Power Generation, vol. 16, no. 1, pp. 33-47, January 2022.

[15] G. Huang, J. Wang, C. Chen, J. Qi, and C. Guo, "Integration of Preventive and Emergency Responses for Power Grid Resilience Enhancement," IEEE Transactions on Power Systems, vol. 32, no. 6, pp. 4451-4463, November 2017.

[16] Y. He, M. Shahidehpour, Z. Li, C. Guo, and B. Zhu, "Robust Constrained Operation of Integrated Electricity-Natural Gas System considering Distributed Natural Gas Storage," IEEE Transactions on Sustainable Energy, vol. 9, no. 3, pp. 1061-1071, July 2018.

[17] F. Lin, Z. Wang, G. Wang, and H. Xin, "Robust Reserve Scheduling Model of Electric Power System Considering WTG De-loading Capability," Automation of Electric Power Systems, vol. 42, no. 19, pp. 64-70, 2018. (In Chinese)

[18] K. Wang, X. Luo, R. Jia, and C. Zhou, "Short-Term Coordinated Scheduling of Wind-Pumped-Hydro-Thermal Power System with Multi-Energy Complementarities," Journal Power System Technology, vol. 44, no. 10, pp. 3631-3640, 2020. (In Chinese)

[19] Z. Chen, Y. Zhang, G. Ma, C. Guo, and J. Zhang, "Two-stage Day-Ahead and Intra-Day Robust Reserve Optimization Considering Demand Response," Automation of Electric Power Systems, vol. 43, no. 24, pp. 67-76, 2019. (In Chinese)

[20] H. Q. Deng, J. Luo, C. C. Li, P. Q. Li, and R. J. Zheng, "Preventive Control Strategy of Cascading Fault considering Safety and Economy," Journal of Electrical and Computer Engineering, vol. 2021, article no. 4554236, 2021.